Ultra-high-energy gamma-ray bubble around microquasar V4641 Sgr

https://doi.org/10.1038/s41586-024-07995-9

Received: 14 March 2024

Accepted: 28 August 2024

[redacted]

R. Alfaro[1], C. Alvarez[2], J. C. Arteaga-Velázquez[3], D. Avila Rojas[1], H. A. Ayala Solares[4], R. Babu[5], E. Belmont-Moreno[1], K. S. Caballero-Mora[2], T. Capistrán[6], A. Carramiñana[7], S. Casanova[8]✉, U. Cotti[3], J. Cotzomi[9], S. Coutiño de León[10], E. De la Fuente[11], D. Depaoli[12], N. Di Lalla[13], R. Diaz Hernandez[7], B. L. Dingus[14], M. A. DuVernois[10], M. Durocher[14], J. C. Díaz-Vélez[10], K. Engel[15], C. Espinoza[1], K. L. Fan[15], K. Fang[10]✉, N. Fraija[6], S. Fraija[6], J. A. García-González[16], F. Garfias[6], A. Gonzalez Muñoz[1], M. M. González[6], J. A. Goodman[15], S. Groetsch[5], J. P. Harding[14], I. Herzog[17], J. Hinton[12], D. Huang[15]✉, F. Hueyotl-Zahuantitla[2], P. Hüntemeyer[5], A. Iriarte[6], V. Joshi[18], S. Kaufmann[19], D. Kieda[20], C. de León[3], J. Lee[21], H. León Vargas[1], J. T. Linnemann[17], A. L. Longinotti[6], G. Luis-Raya[19], K. Malone[22], O. Martinez[9], J. Martínez-Castro[23], J. A. Matthews[24], P. Miranda-Romagnoli[25], J. A. Morales-Soto[3], E. Moreno[9], M. Mostafá[26], A. Nayerhoda[8], L. Nellen[27], M. Newbold[20], M. U. Nisa[17], R. Noriega-Papaqui[25], L. Olivera-Nieto[12], N. Omodei[13], M. Osorio[6], Y. Pérez Araujo[1], E. G. Pérez-Pérez[19], C. D. Rho[28], D. Rosa-González[7], E. Ruiz-Velasco[12], H. Salazar[9], D. Salazar-Gallegos[17], A. Sandoval[1], M. Schneider[15], J. Serna-Franco[1], A. J. Smith[15], Y. Son[21], R. W. Springer[20], O. Tibolla[19], K. Tollefson[17], I. Torres[7], R. Torres-Escobedo[29], R. Turner[5], F. Ureña-Mena[7], E. Varela[9], L. Villaseñor[9], X. Wang[5]✉, I. J. Watson[21], E. Willox[15], S. Yun-Cárcamo[15] & H. Zhou[29]

Microquasars are laboratories for the study of jets of relativistic particles produced by accretion onto a spinning black hole. Microquasars are near enough to allow detailed imaging of spatial features across the multiwavelength spectrum. The recent extension measurement of the spatial morphology of a microquasar, SS 433, to TeV gamma rays[1] localizes the acceleration of electrons at shocks in the jet far from the black hole[2]. V4641 Sagittarii (V4641 Sgr) is a similar binary system with a black hole and B-type main-sequence companion star and has an orbit period of 2.8 days (refs. 3,4). It stands out for its super-Eddington accretion[5] and for its radio jet, which is one of the fastest superluminal jets in the Milky Way. Previous observations of V4641 Sgr did not report gamma-ray emission[6]. Here we report TeV gamma-ray emission from V4641 Sgr that reveals particle acceleration at similar distances from the black hole as SS 433. Furthermore, the gamma-ray spectrum of V4641 Sgr is among the hardest TeV spectra observed from any known gamma-ray source and is detected above 200 TeV. Gamma rays are produced by particles, either electrons or protons, of higher energies. Because energetic electrons lose energy more quickly the higher their energy, such a spectrum either very strongly constrains the electron-production mechanism or points to the acceleration of high-energy protons. This suggests that large-scale jets from microquasars could be more common than previously expected and that they could be a notable source of galactic cosmic rays[7–9].

Observations from 2015 to 2022 by the High-Altitude Water Cherenkov (HAWC) Observatory[10] have revealed notable gamma-ray emission coincident with the location of V4641 Sgr, as shown in Fig. 1. The excess over the estimated cosmic-ray background flux reaches a maximum significance of 8.8σ above 1 TeV and 5.2σ above 100 TeV. After ruling out an association with extragalactic background sources and other high-energy sources in the galaxy, we conclude that V4641 Sgr is the probable source of the observed gamma-ray excess (see details in Methods).

On the basis of a systematic multisource analysis method on a 3° radius region of interest (ROI) around the gamma-ray emission, the excess may be described as either two point-like sources or one extended source with an asymmetric Gaussian distribution (see details in Methods). The present statistics do not allow us to distinguish between the two spatial models. When adopting a two-point-source model, the northern source and the southern source are detected at 8.1σ and 6.7σ, respectively The 95% upper limits on the extensions of the two sources are found to be 0.17° and 0.23°, respectively, when fitting

---

A list of affiliations appears at the end of the paper.

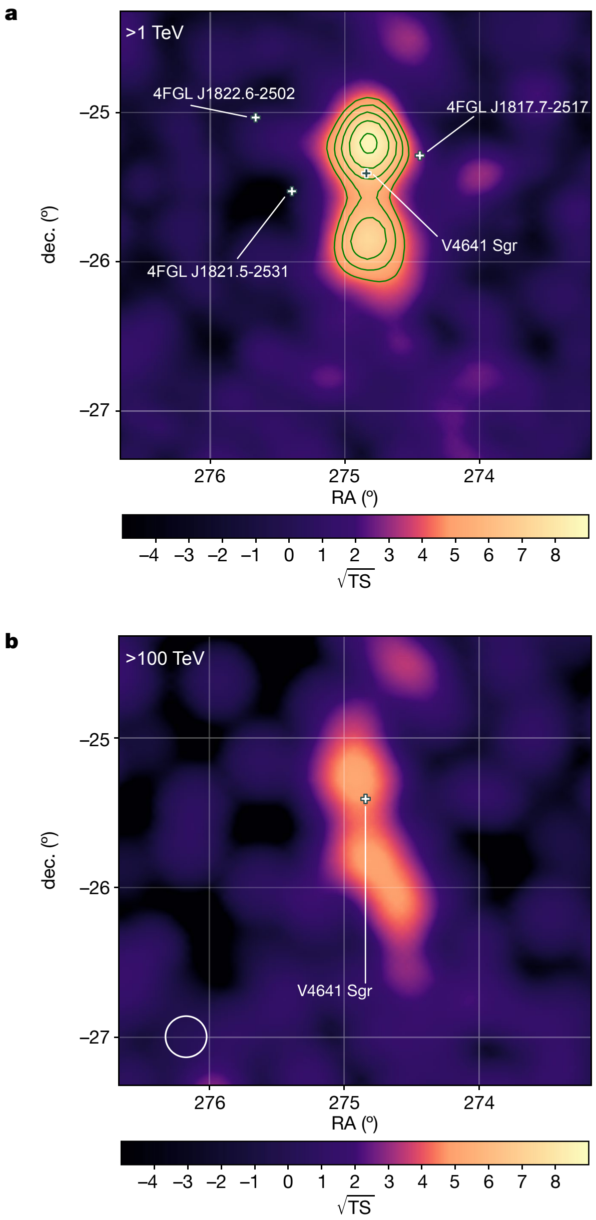

Fig. 1 | Significance map around the V4641 Sgr region. a, For events with measured energy greater than 1 TeV. The value TS refers to the likelihood ratio test statistic described in equation (1). The green contours indicating significance are mapped to $\sqrt{\mathrm{TS}}$ values ranging from 4.5 to 8.5, increasing inwards at intervals of one from the outermost contour to the innermost. The crosses represent the best-fit locations from the model with two point sources. **b**, Significance map (of the same region) including only events with measured energy greater than 100 TeV. The white circle represents the angular resolution at a radius corresponding to 68% event containment (0.17°) at this energy range. The V4641 Sgr location is taken from ref. 4. These significance maps are made by assuming a point-source hypothesis and a power-law spectrum with the best-fit index $\alpha = -2.2$.

a Gaussian spatial template to the data around each source over the entire energy range. For comparison, the HAWC point-spread function at the declination of the source is 0.2° at energies greater than 30 TeV. The angular separations between the binary and the northern and southern gamma-ray sources are 0.23° and 0.46°, which correspond to about 30 pc and about 55 pc, respectively, when assuming a source distance of 6.6 kpc (ref. 4). When adopting a single-source model, we find that a point-like source template is disfavoured at 8.3σ with respect to an asymmetric extended-source template. The extension of the asymmetric source is found to be 0.54°, corresponding to about 70 pc. This is much larger than the size of the binary system, implying that the gamma-ray emission comes from a region more extended than the central binary.

Under the model with two point sources from a physically grounded perspective, the excess spectrum extends up to 217 TeV without any observable indication of a cut-off (for the best-fit results of the model with a single asymmetric extended source, see Methods). The spectrum above 1 TeV is best described by a power law, $\mathrm{d}N/\mathrm{d}E = N_0(E/E_0)^{\alpha}$, in which $E_0 = 47$ TeV is selected to minimize the correlation between parameters owing to the choice of the spectral model. Table 1 lists the best-fit values of N_0 and α for the northern and southern sources. We note that the exceptionally hard spectrum, $\alpha = -2.2$, makes V4641 Sgr one of the hardest ultra-high-energy sources ever measured. Figure 2 compares the spectra of the two sources. Despite being 0.69 ± 0.04° (about 80 pc) away from each other, the two sources present almost identical flux amplitudes and spectral indices, hinting that they probably share a common origin. Considering that no other plausible multiwavelength counterparts can be identified and that the two point-like sources present remarkably similar spectra while being physically distant, the origin of the HAWC excess is probably connected to V4641 Sgr and could be because of persistent large-scale outflows from the system, each of which we refer to as a bubble.

Interaction of large-scale jets with the interstellar medium (ISM) may induce high-energy radiation. So far, SS 433 is the only microquasar with very-high-energy (VHE; 0.1–100 TeV) gamma-ray emission observed from the lobes[1,2]. At a distance of 6.6 kpc for V4641 Sgr, the physical separation between each of the two sources and the central object is on the order of tens of parsecs. Our observation implies that V4641 Sgr could be closely analogous to SS 433 (ref. 1), which has long been proposed, based on optical and X-ray observations of the flares[11–13]. The ratio of the TeV gamma-ray power and the Eddington luminosity of this source is an order of magnitude higher than that of SS 433, suggesting that large-scale outflows from microquasars may carry high kinetic power and be efficient particle accelerators.

Persistent VHE gamma-ray emission from microquasars can be expected from accelerated electrons inverse Compton scattering off low-energy photons (leptonic scenario) and/or from the decay of neutral pions, which are produced by the interaction of protons and nuclei (hadronic scenario)[14,15].

A leptonic scenario is challenging for the following reasons. First, a fast outflow is needed to accelerate electrons to 200 TeV and above. The acceleration time, $t_{\mathrm{acc}} \approx 10D_{\mathrm{B}}(E_e)/\upsilon_{\mathrm{sh}}^2$, needs to be shorter than the cooling time owing to synchrotron radiation in a magnetic field B, $t_{\mathrm{cooling}} \approx 600(E_e/200\ \mathrm{TeV})^{-1}(B/10\ \mu\mathrm{G})^{-2}$ years, yielding a shock velocity, $\upsilon_{\mathrm{sh}}/c > 0.02(E_e/200\ \mathrm{TeV})(B/10\ \mu\mathrm{G})^{1/2}$. Here $D_{\mathrm{B}}(E_e) = R_{\mathrm{L}}c/3$ is the Bohm diffusion coefficient and R_{L} is the Larmor radius of the particle. Second, electrons at such high energies cool so quickly that they can barely travel over 100 pc. The cooling time is much shorter than the diffusion time, $R^2/(2D) \approx 1{,}000/\eta$ years, in which $R \approx 100$ pc, $D(200\ \mathrm{TeV}) \approx \eta 10^{30}\ \mathrm{cm}^2\ \mathrm{s}^{-1}$ and $\eta \ll 1$. For these evaluations, we have used a magnetic field strength comparable with that in the jets of SS 433 (ref. 1). Future X-ray observations of the VHE emission site are needed to constrain the field strength.

In the hadronic scenario, protons are accelerated to PeV energies and interact with the ambient gas, producing neutral pions that quickly decay into gamma rays. Extended Data Fig. 3 shows the gas distribution near the gamma-ray excess detected by HAWC. To account for both the southern and northern HAWC sources, we require a total proton energy $W_{\mathrm{p}} \approx 1 \times 10^{50}$ erg for these two sources. The protons could be accelerated at the termination shock, at which the jets interact with the ISM, or along the jets and subsequently transported to the HAWC sources. We assume that each HAWC source has a radius of 20 pc, which corresponds to the upper limit on the source radius of 0.2° at the 95% confidence level, and consider escape owing to diffusion for two cases: diffusion as inferred at GeV energies from the cosmic-ray secondaries

Table 1 | Best-fit parameters for a model with two point sources

Source name	RA (°)	dec. (°)	N_0 ($\times 10^{-16}$ cm^{-2} TeV^{-1} s^{-1})	Index (α)	Extension upper limit at 95% confidence level (°)	Physical distance to the black hole (distance: 6.6 kpc)
Southern	274.82 ± 0.04	−25.87 ± 0.03	$2.4^{+0.6}_{-0.5}$(stat.)$^{+0.2}_{-0.5}$(syst.)	−2.2 ± 0.2(stat.)$^{+0.07}_{-0.02}$(syst.)	0.23	0.46° ≈ 55 pc
Northern	274.82 ± 0.03	−25.18 ± 0.02	$2.6^{+0.5}_{-0.4}$(stat.) ± 0.4(syst.)	−2.2 ± 0.2(stat.)$^{+0.07}_{-0.05}$(syst.)	0.17	0.23° ≈ 30 pc

The optimal pivot energy, E_0, is 47 TeV for both sources.

or the much slower Bohm diffusion. For 1-PeV protons, the escape time is then 40 years or 4,000 years, respectively. The energy required in the former case exceeds the Eddington luminosity assuming that protons are accelerated with the same spectrum from 1 GeV to 1 PeV, but is only a small fraction of the Eddington luminosity in the latter case. We also note that the power channelled into the kinetic energy of the jets might easily exceed the Eddington luminosity, as testified by the super-Eddington flares[16].

The detection of greater than 100-TeV photons indicates that microquasars could be protonic PeVatrons. A smoking gun for this hadronic PeVatron scenario could be the detection of high-energy neutrinos from V4641 Sgr. The neutrinos accompanying the gamma-ray emission have a flux below the present IceCube sensitivity[17], although future experiments could detect them.

Large-scale jets have been found in several microquasars[18–22]. They carry the bulk of the liberated accretion power of the compact objects and are local analogues of Fanaroff–Riley type II active galaxies. The interaction of large-scale jets and the ambient medium is suggested to produce shock-ionized nebulae such as W50 (ref. 23) and to explain the bubbles around ultraluminous X-ray sources, the most luminous class of extra-nuclear X-ray emitters[22,24–26]. The formation of large-scale jets and their connection with extended nebulae or bubbles around microquasars remains poorly known because of the rarity of such objects. Detection of extended jets is challenging, both because the outflows could be radiatively inefficient, and thus ‘dark’ in optical/ultraviolet/X-ray[20], and because a pair of extragalactic sources located on either side of a microquasar could cause a false association in radio and X-ray wavelengths[27].

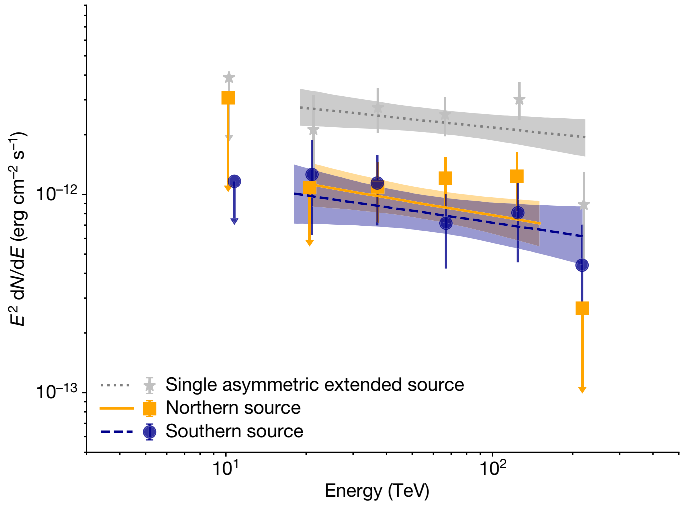

Fig. 2 | Spectral energy distribution of the gamma-ray emission. Differential spectrum weighted by E^2 for the northern and southern sources in a model with two point sources and for the asymmetric extended source in a model with a single asymmetric extended source. The shaded regions indicate the best-fit spectra and 1σ statistical uncertainties when fitting a single-power-law model to the data from 10 to >200 TeV. The markers correspond to the best-fit values and their 1σ statistical uncertainties obtained when fitting a single-power-law model to data in individual energy bins. The chosen energy range for plotting the spectrum is specified in the Methods.

With a jet luminosity exceeding $L_{\rm edd} \approx 10^{39}$ erg s^{-1} (ref. 11), the gamma-ray excess observed by HAWC aligns with the expectation that V4641 Sgr powers a wind-driven nebula or jet-driven radio lobes at a scale of $R \approx 0.76(L_{\rm jet}/n_0 m_{\rm p})^{1/5} t^{3/5} = 110$ pc, in which $m_{\rm p}$ is the mass of the proton, $n_0 \approx 1$ cm^{-3} is the ambient gas density, which is derived from the column density in the directions of the VHE lobes (see Methods) and also comparable with the average of the ISM gas density, and $t \approx 1$ Myr is the estimated age of the source[28]. The discovery of the ultra-high-energy gamma-ray bubble around V4641 Sgr supports the long-standing hypothesis that this source shares similarities with SS 433 and suggests that the super-Eddington outflows could power steady, large-scale jets.

Compared with SS 433, the gamma-ray spectrum of V4641 Sgr is harder and the large-scale jets have not been observed in other wavelengths. Although both protons and electrons could be accelerated in the V4641 Sgr system, the dominant radiation mechanism, whether it is leptonic or hadronic, depends on the surrounding conditions, such as gas density and magnetic fields. These differences in ambient conditions may explain the observational discrepancies between SS 433 and V4641 Sgr.

The large-scale jets of microquasars may play an important role in the production of galactic cosmic rays. Microquasar jets have long been suggested as cosmic-ray sources, although their contribution to the galactic cosmic-ray flux is unknown. As a result of the uncertainties in the duty cycle, kinetic energy output and composition of the microquasar jets, this contribution may vary from 0.1% to 100% (refs. 8,9,29,30). Our observation favours microquasar jets as extraordinary cosmic-ray sources by suggesting the existence of large-scale steady jets, thereby having a long duty cycle, and by finding V4641 Sgr to be an emitter of 200-TeV photons, such that it is, therefore, a plausible accelerator of PeV cosmic-ray protons.

Online content

Any methods, additional references, Nature Portfolio reporting summaries, source data, extended data, supplementary information, acknowledgements, peer review information; details of author contributions and competing interests; and statements of data and code availability are available at https://doi.org/10.1038/s41586-024-07995-9.

1. Abeysekara, A. et al. Very-high-energy particle acceleration powered by the jets of the microquasar SS 433. *Nature* **562**, 82–85 (2018).
2. Abdalla, H. et al. Acceleration and transport of relativistic electrons in the jets of the microquasar SS 433. *Science* **383**, 402–406 (2024).
3. MacDonald, R. K. D. et al. The black hole binary V4641 Sagitarii: activity in quiescence and improved mass determinations. *Astrophys. J.* **784**, 2 (2014).
4. Gaia, C. et al. Gaia Data Release 2. Summary of the contents and survey properties. *Astron. Astrophys.* **616**, A1 (2018).
5. in ’t Zand, J. et al. SAX J1819.3-2525. International Astronomical Union Circular, No. 7119, #1 (1999).
6. Abdalla, H. et al. A search for very high-energy flares from the microquasars GRS 1915+105, Circinus X-1, and V4641 Sgr using contemporaneous H.E.S.S. and RXTE observations. *Astron. Astrophys.* **612**, A10 (2018).
7. Escobar, G. J., Pellizza, L. & Romero, G. E. Cosmic-ray production from neutron escape in microquasar jets. *Astron. Astrophys.* **650**, A136 (2021).
8. Fender, R., Maccarone, T. & Van Kesteren, Z. Energization of interstellar media and cosmic ray production by jets from X-ray binaries. *Mon. Not. R. Astron. Soc.* **360**, 1085–1090 (2005).
9. Romero, G. E. & Vila, G. S. The proton low-mass microquasar: high-energy emission. *Astron. Astrophys.* **485**, 623–631 (2008).

10. Abeysekara, A. et al. The High-Altitude Water Cherenkov (HAWC) observatory in México: the primary detector. *Nucl. Instrum. Methods Phys. Res. A* **1052**, 168253 (2023).
11. Revnivtsev, M., Sunyaev, R., Gilfanov, M. & Churazov, E. V4641Sgr—a super-Eddington source enshrouded by an extended envelope. *Astron. Astrophys.* **385**, 904–908 (2002).
12. Lindstrøm, C. et al. New clues on outburst mechanisms and improved spectroscopic elements of the black hole binary V4641 Sagittarii. *Mon. Not. R. Astron. Soc.* **363**, 882–890 (2005).
13. Gallo, E., Plotkin, R. M. & Jonker, P. G. V4641 Sgr: a candidate precessing microblazar. *Mon. Not. R. Astron. Soc. Lett.* **438**, L41–L45 (2013).
14. Aharonian, F. & Atoyan, A. Gamma rays from galactic sources with relativistic jets. *New Astron. Rev.* **42**, 579–584 (1998).
15. Heinz, S. & Sunyaev, R. Cosmic rays from microquasars: a narrow component to the CR spectrum? *Astron. Astrophys.* **390**, 751–766 (2002).
16. Aharonian, F. A. *Very High Energy Cosmic Gamma Radiation. A Crucial Window on the Extreme Universe* (World Scientific, 2004).
17. IceCube Collaboration. Observation of high-energy neutrinos from the galactic plane. *Science* **380**, 1338–1343 (2023).
18. Margon, B. Observations of SS 433. *Annu. Rev. Astron. Astrophys.* **22**, 507–536 (1984).
19. Corbel, S. et al. Large-scale, decelerating, relativistic X-ray jets from the microquasar XTE J1550-564. *Science* **298**, 196–199 (2002).
20. Gallo, E. et al. A dark jet dominates the power output of the stellar black hole Cygnus X-1. *Nature* **436**, 819–821 (2005).
21. Sell, P. H. et al. Parsec-scale bipolar X-ray shocks produced by powerful jets from the neutron star Circinus X-1. *Astrophys. J. Lett.* **719**, L194–L198 (2010).
22. Pakull, M. W., Soria, R. & Motch, C. A 300-parsec-long jet-inflated bubble around a powerful microquasar in the galaxy NGC 7793. *Nature* **466**, 209–212 (2010).
23. Fabrika, S. The jets and supercritical accretion disk in SS 433. *Astrophys. Space Phys. Rev.* **12**, 1–152 (2004).
24. Pakull, M. W. & Mirioni, L. Bubble nebulae around ultraluminous X-ray sources. In *Proc. Winds, Bubbles, and Explosions: A Conference to Honor John Dyson* (eds Arthur, S. J. & Henney, W. J.) 197–199 (2003).
25. Berghea, C. T. et al. Detection of a radio bubble around the ultraluminous X-ray source Holmberg IX X-1. *Astrophys. J.* **896**, 117 (2020).
26. Kaaret, P., Feng, H. & Roberts, T. P. Ultraluminous X-ray sources. *Annu. Rev. Astron. Astrophys.* **55**, 303–341 (2017).
27. Mirabel, I. F. & Rodríguez, L. F. Sources of relativistic jets in the galaxy. *Annu. Rev. Astron. Astrophys.* **37**, 409–443 (1999).
28. Salvesen, G. & Pokawanvit, S. Origin of spin–orbit misalignments: the microblazar V4641 Sgr. *Mon. Not. R. Astron. Soc.* **495**, 2179–2204 (2020).
29. Heinz, S. & Sunyaev, R. A. Cosmic rays from microquasars: a narrow component to the CR spectrum? *Astron. Astrophys.* **390**, 751–766 (2002).
30. Cooper, A. J., Gaggero, D., Markoff, S. & Zhang, S. High-energy cosmic ray production in X-ray binary jets. *Mon. Not. R. Astron. Soc.* **493**, 3212–3222 (2020).

---

[1]Instituto de Física, Universidad Nacional Autónoma de México, Ciudad de México, Mexico. [2]Universidad Autónoma de Chiapas, Tuxtla Gutiérrez, Mexico. [3]Universidad Michoacana de San Nicolás de Hidalgo, Morelia, Mexico. [4]Department of Physics, Pennsylvania State University, University Park, PA, USA. [5]Department of Physics, Michigan Technological University, Houghton, MI, USA. [6]Instituto de Astronomía, Universidad Nacional Autónoma de México, Ciudad de México, Mexico. [7]Instituto Nacional de Astrofísica, Óptica y Electrónica, Puebla, Mexico. [8]Institute of Nuclear Physics Polish Academy of Sciences, Kraków, Poland. [9]Facultad de Ciencias Físico Matemáticas, Benemérita Universidad Autónoma de Puebla, Puebla, Mexico. [10]Department of Physics, University of Wisconsin–Madison, Madison, WI, USA. [11]Departamento de Física, Centro Universitario de Ciencias Exactas e Ingenierias, Universidad de Guadalajara, Guadalajara, Mexico. [12]Max Planck Institute for Nuclear Physics, Heidelberg, Germany. [13]Department of Physics, Stanford University, Stanford, CA, USA. [14]Physics Division, Los Alamos National Laboratory, Los Alamos, NM, USA. [15]Department of Physics, University of Maryland, College Park, MD, USA. [16]Tecnologico de Monterrey, Escuela de Ingeniería y Ciencias, Monterrey, Mexico. [17]Department of Physics and Astronomy, Michigan State University, East Lansing, MI, USA. [18]Erlangen Centre for Astroparticle Physics, Friedrich-Alexander-Universität Erlangen-Nürnberg, Erlangen, Germany. [19]Universidad Politecnica de Pachuca, Pachuca, Mexico. [20]Department of Physics and Astronomy, University of Utah, Salt Lake City, UT, USA. [21]University of Seoul, Seoul, Korea. [22]Space Science and Applications Group, Los Alamos National Laboratory, Los Alamos, NM, USA. [23]Centro de Investigación en Computación, Instituto Politécnico Nacional, Mexico City, Mexico. [24]Department of Physics and Astronomy, University of New Mexico, Albuquerque, NM, USA. [25]Universidad Autónoma del Estado de Hidalgo, Pachuca, Mexico. [26]Department of Physics, Temple University, Philadelphia, PA, USA. [27]Instituto de Ciencias Nucleares, Universidad Nacional Autónoma de Mexico, Ciudad de México, Mexico. [28]Department of Physics, Sungkyunkwan University, Suwon, Korea. [29]Tsung-Dao Lee Institute, Shanghai Jiao Tong University, Shanghai, China. ✉e-mail: sabrina.casanova@ifj.edu.pl; kefang@physics.wisc.edu; dezhih@umd.edu; xwang32@mtu.edu

Methods

HAWC data

The HAWC Observatory consists of 300 water Cherenkov detectors located on the slope of the Sierra Negra volcano in Puebla, Mexico, at an elevation of 4,100 m (ref. 10). Each detector has four upward-facing photomultiplier tubes (PMTs) at its bottom to collect the Cherenkov light produced by secondary air-shower particles in the water. By using the charge and time information recorded by the PMTs, we can reconstruct the properties of the primary particles. Recently, with better reconstruction algorithms and gamma/hadron separation, the sensitivity of the HAWC Observatory has been improved by a factor of 2–4 (depending on the declination and energy range).

This analysis uses approximately 2,400 days of data collected between 26 November 2014 and 27 June 2022, reconstructed using recently improved algorithms[31]. The HAWC data are binned according to the fraction of available PMTs hit and reconstructed energy[32]; air-shower events with higher energies typically trigger more PMTs. Simultaneously, we differentiate between events with shower cores landing exclusively on the array (on-array events) and those with cores landing off the array (off-array events). Only on-array events are used in this work. Events with the highest fraction of PMTs hit have the highest energies and the best angular resolutions, with values of 0.18° (68% containment radius) or better.

Likelihood analysis

We performed a maximum-likelihood analysis using the HAWC plugin to the Multi-Mission Maximum Likelihood (3ML) software framework[33–35]. This method obtains the best-fit parameters by means of maximum likelihood for a model with a given spatial and spectral assumption convolved with the detector response functions. The background is estimated by the 'direct integration' method[36,37]. For events with a larger fraction of PMT hits, we also used the 'background randomization' method (as described in ref. 32) alongside 'direct integration' to spatially smooth the background.

The likelihood ratio test statistic (TS) is used to compare the two given models, defined as:

$$\mathrm{TS} = -2\ln\left(\frac{L_{\mathrm{null}}}{L_{\mathrm{alt}}}\right), \quad (1)$$

in which L_{alt} is the maximum likelihood of the alternative hypothesis (background + source model) and L_{null} is the likelihood of the null hypothesis (background only).

In the analysis, we used a circular ROI with a radius of 3°, centred at RA = 274.92°, dec. = −25.82°. To explore gamma-ray emission within the ROI, we conducted a systematic multisource analysis method inspired by the Fermi-LAT[38]. As the latitude of the centre of the ROI is 5° away from the galactic plane, background emission owing to the galactic diffuse emission and unresolved sources on the galactic plane is negligible. Furthermore, because the source is so isolated, unlike SS 433 and other sources on the galactic plane that could be affected by galactic diffuse emission, it serves as an excellent laboratory for studying the source emission independently. Therefore, we begin with a model consisting of a single point source and a simple-power-law spectral assumption. Then, we add point sources until there is no excess with significance greater than 4σ. Following this, we test the extension of each added point source sequentially to obtain the best morphological description of the emission. We further explore two distinct spectral models for the emission: the simple-power-law spectrum ($\mathrm{d}N/\mathrm{d}E = N_0(E/E_0)^{\alpha}$) and the log-parabola spectrum ($\mathrm{d}N/\mathrm{d}E = N_0(E/E_0)^{\alpha-\beta\log(E/E_0)}$). The pivot energy, E_0, is determined by minimizing the correlation between the flux normalization, N_0, and the spectral index, α. The pivot energy is fixed at 47 TeV for models with two sources while letting the other parameters float. Through this comprehensive multisource analysis, we identified a model with two point sources as the best model to describe the observed gamma-ray excess. Because this analysis is for a targeted, specific region, we further explored several alternative models involving asymmetric extended sources. A single asymmetric extended-source model also provides a satisfactory description of our data.

The value ΔTS is used to compare nested models, such as the single-point-source model and the model with two point sources. The Bayesian information criterion (BIC[39,40]) and Akaike information criterion (AIC[41]) are used for non-nested model comparisons. In the model with two point sources, the ΔTS between the simple-power-law spectrum and the log-parabola spectrum is 0 for the southern source and 6 for the northern source; for the model with a single asymmetric extended source, the ΔTS between the two spectral models is 6. Given that the values are 0 and 2.4σ, respectively, for one extra free parameter—both of which are $<4\sigma$—this comparison suggests that there is no notable curvature in the energy spectrum in the present HAWC data. The upper limits at the 95% confidence level for the Gaussian width of the sources in the two-source model are 0.23° and 0.17° for the southern source and the northern source, respectively.

From Extended Data Table 1, it is evident that the single-point-source model is disfavoured compared with the model with two point sources with a ΔTS value of 78, corresponding to an 8.1σ significance, considering four degrees of freedom. Furthermore, the comparison between a single symmetric extended-source model and a model with a single asymmetric extended source is unfavourable based on both ΔTS and ΔBIC assessments. It is noteworthy that the ΔBIC value incurs substantial penalties resulting from the two extra parameters and the large number of pixels in the ROI associated with the asymmetric extended-source model. Moreover, the present HAWC data do not allow us to differentiate between the model with two point sources and the model with a single asymmetric extended source. The presence of an extra free parameter and the involvement of nearly 100,000 pixels in the fitting process naturally leads to a substantial ΔBIC, disfavouring the model with two point sources. If we ignore the penalty originating from the pixel count in the fit and consider instead the AIC, the model with a single asymmetric extended source only exhibits a marginal improvement with a ΔAIC value of one. This small difference emphasizes the inability to distinguish between the two models. Given the best-fit eccentricity of 0.98 ± 0.01 (for other parameters, see Extended Data Table 2), it remains plausible that the occurrence of the asymmetric extended source could be attributed to the presence of two closely overlapping sources that cannot be definitively distinguished. We also tested models fixed at the black hole location for events above 56 TeV. Compared with the model with a single extended source, a single point source is disfavoured with ΔTS = 34, equivalent to 5.9σ with one degree of freedom.

Energy-range study/upper limit on the observed photon energy

To estimate the maximum energy of the gamma-ray emission detected by the HAWC Observatory, we applied a forward-folding method similar to Abeysekara et al.[42,43]. In this method, we multiply a step function by the best-fit energy spectral model (a simple-power-law spectrum). Keeping the boundary of the function floating and all the other parameters fixed in the fitting, we can obtain the maximum and minimum energy by comparing the log-likelihood value with our best-fit model. The energy value at which the log-likelihood value decreases by 1σ is chosen as the minimum E_{max} energy for the detected gamma rays. On the basis of the energy-range study, the present measurement of the gamma-ray excess observed by HAWC extends from 18 TeV to 217 TeV for the southern source, whereas the northern source is observed from 21 TeV to 150 TeV. Both sources share identical spectral indices of −2.2, as shown in Fig. 2.

Systematic uncertainties

The contribution to the systematic uncertainties from the detector effects on the flux normalization of the TeV emission from V4641 Sgr is less than ±20% of the nominal value. The index of the TeV emission from V4641 Sgr changes by <3% because of detector systematics. These systematic uncertainties are determined as described in ref. 32, which includes the absolute quantum efficiency of the PMTs, charge resolution and threshold of the PMTs, changes to PMT efficiency over time and how late light in the air shower is treated. Uncertainties from each category are investigated and summed in quadrature to estimate the total systemic uncertainties.

We also studied the pointing accuracy. In the 3HWC catalogue paper[44], we quote the absolute pointing uncertainty of HAWC as 0.15° for sources at −10° or +50° declination and 0.3° for sources at declinations of −20° or +60°. With a better reconstruction algorithm, we have improved the pointing uncertainty. To validate this improvement, we conducted a series of tests.

We compare the measured declination of HAWC sources with the declination of their potential TeV counterparts as determined by the High Energy Stereoscopic System (H.E.S.S.), chosen as a representative imaging atmospheric Cherenkov telescope experiment. The source locations and their uncertainties were obtained from the H.E.S.S. galactic plane survey (HGPS) paper[45]. Extended Data Fig. 1 shows the comparison between the declination of sources detected by HAWC and H.E.S.S., revealing substantial agreement between the two experiments for declinations ranging from −10° to −30°. The error bars in the plot indicate uncertainties derived from the combined errors of HAWC and H.E.S.S., calculated in quadrature. The H.E.S.S. data, sourced from the HGPS paper[45], may reflect variations in the observation times of individual sources. This comparison confirms the consistency and reliability of HAWC's pointing.

Source associations

We searched for possible associations with the gamma-ray excess in high-energy catalogues. Unlike in radio and X-ray, a chance superposition of extragalactic background sources can be easily ruled out at 200 TeV. This is because most photons at this energy will be attenuated as a result of pair production with background radiation fields when travelling across the Milky Way and over extragalactic distances. At TeV energies, we found no known source within 3° of the HAWC point sources. At GeV energies, three sources from the 4FGL catalogue[46] are found within the 0.5° radius of the HAWC point sources, but all of them are outside the 4.5σ excess region (see Fig. 1). One of the three sources is a distant galaxy and the other two have no known associations. At X-ray wavelengths, we searched for counterparts in the galactic Master X-Ray Catalog from the NASA HEASARC database (https://heasarc.gsfc.nasa.gov/W3Browse/all/xray.html) and several X-ray binary catalogues, including the High-Mass X-Ray Binaries Catalog (HMXBCAT)[47], the Low-Mass X-Ray Binaries Catalog (LMXBCAT)[48], the Ritter Low-Mass X-Ray Binaries Catalog (RITTERLMXB)[49], the X-Ray Binaries Catalog (XRBCAT)[50] and the Integral IBIS 9-Year Galactic Hard X-Ray Survey Catalog (INTIBISGAL)[51]. Only a handful of sources are found in the vicinity, including IGR J18170-2511, XTE J1818-245, AX J1824.5-2451 (J1824-2452) and SAX J1810.8-2609. Three galactic sources are located within 0.5° of the northern and southern sources, namely, V4641 Sgr, IGR 1819.3-2542 and SWIFT J1818.7-2553. The last two are known to be associated with V4641 Sgr (refs. 52,53).

Time-dependent study

V4641 Sgr is well known for its violent X-ray outbursts. To study the time dependency of the VHE gamma-ray emission, we carried out two distinct tests. First, we split the data into two halves. The first half of the data runs from November 2014 to May 2018 and the second half from May 2018 to June 2022; the significance and location of the gamma-ray excess do not show marked differences between the two halves. For the second test, we selected approximately 180 days of data during four recorded X-ray bursts from the Monitor of All-sky X-ray Image (MAXI) telescope[54]. We used the online Bayesian Blocks analysis tool on the MAXI website to select approximately 180 days of data during which V4641 Sgr was in an X-ray outburst state (http://maxi.riken.jp/mxondem/). We searched for excess gamma-ray emission based on this combined dataset. Extended Data Table 3 details the dates chosen for the four confirmed outbursts. No marked excess is observed in the data for the selected time period. The X-ray emission detected by Chandra during the 2020 outburst[55] exhibited substantially higher flux compared with the consistent gamma-ray flux observed by HAWC. Furthermore, there was no noticeable increase in gamma-ray emissions during the periods corresponding to the X-ray outbursts. This disparity indicates that the gamma-ray and X-ray emissions are probably not because of the same particle population. In summary, the HAWC-measured radiation shows no variation over different time periods, including recorded X-ray outbursts.

Multiwavelength observation of V4641 Sgr

V4641 Sgr is famous for its super-Eddington X-ray outbursts. Its most notable flare happened in September 1999, when the flux level reached 12.2 Crab, corresponding to a 1–10-keV luminosity of $(3\text{–}4) \times 10^{39}$ erg s^{-1} (ref. 56). Some of the X-ray outbursts present lower luminosity. One explanation for the lower flux is that the central engine is potentially obscured by an optically thick outflow[55–57], in which case the intrinsic X-ray luminosity was higher than observed.

H.E.S.S. conducted VHE observations of V4641 Sgr simultaneously with the Rossi X-ray Timing Explorer (RXTE) in 2018, accumulating an overall livetime of 1.76 h, yielding a non-detection in gamma rays[6]. They reported an upper limit of the integral flux above 240 GeV as $I(E > 240\ \text{GeV}) < 4.5 \times 10^{-12}\ \text{cm}^{-2}\ \text{s}^{-1}$, which is consistent with HAWC's observation of the integral flux above 10 TeV of $I(E > 10\ \text{TeV}) = 2.60^{+0.26}_{-0.05} \times 10^{-12}\ \text{cm}^{-2}\ \text{s}^{-1}$. We note that the H.E.S.S. analysis only considered a single potential point source at the location of the binary, whereas the upper limit from HAWC is determined using the best-fit differential flux under the assumption of two point sources.

Radio observations by the Very Large Array (VLA) of the September 1999 outburst events of V4641 Sgr resolved a bright, jet-like radio structure[58]. These radio observations suggest that V4641 Sgr might be a galactic 'microblazar', which means that its jet inclination is small or even aligned with the line of sight[13,59,60].

Extended Data Fig. 2 presents a sketch of the binary system. The inclination angle, i, of V4641 Sgr, defined as the direction of the normal to the binary orbital plane with respect to the observer's line of sight, is about 72.3° ± 4.1° (ref. 3). In a standard system, in which the disk is aligned with the orbital plane and the jets are perpendicular to the disk, this angle would be similar to the jet angle, θ, defined as the angle of the jets with respect to the line of sight. It is not yet understood why the transient radio jets of V4641 Sgr present an unusual $\theta < 12°$ (ref. 59). The gamma-ray sources, on the other hand, would be consistent with a scenario involving jets that are perpendicular to the accretion disk.

The absence of detectable persistent X-ray emission associated with the gamma-ray lobes could be because of the low surface brightness of the X-ray counterpart, which emits synchrotron radiation from secondary electrons, a lack of deep X-ray observations of the large-scale jets or a combination of both factors.

Gas distribution

In the hadronic scenario, high-energy protons interact with the ambient gas, resulting in the production of gamma rays through the decay process $\pi^0 \rightarrow \gamma\gamma$. The molecular hydrogen survey[61,62] and the HI4PI 21-cm line emission survey of atomic hydrogen[63–65] provide the gas column density from the direction of the V4641 Sgr region.

To obtain a realistic estimate of the gas density in the region of V4641 Sgr, we need to integrate the gas survey cubes over the range of velocities corresponding to the distance of V4641 Sgr and then divide by the velocity interval. The V4641 Sgr distance of 6.6 kpc roughly corresponds to a velocity of 90–100 km s^{-1} according to the galactic rotation velocity curve[66]. Integrating the HI spectra over a range of velocities between 70 km s^{-1} and 120 km s^{-1} (this spread in velocities includes, for instance, possible internal turbulent motions of the gas), the first momenta yield $N_{\mathrm{H}} = 7.4 \times 10^{19}$ cm^{-2} and $N_{\mathrm{H}} = 3.9 \times 10^{19}$ cm^{-2} for the southern and northern lobes, respectively. We also examined the molecular gas distribution at the locations of the two HAWC lobes by integrating the molecular hydrogen cubes over the velocity range 70–120 km s^{-1} (refs. 61,62). As far as the molecular hydrogen is concerned, the maps contain high levels of background fluctuation noise such that we cannot confirm the presence of any emission from hadrons colliding off molecular hydrogen targets.

Assuming a radius of approximately 20 pc for each lobe from an upper limit of 0.2° at the 95% confidence level for the Gaussian width of the sources, the gas density, n, is 1 cm^{-3} and 0.5 cm^{-3} for the south and north lobes, respectively.

VHE emission owing to hadronic interactions

In the hadronic scenario, the interaction of high-energy protons with the surrounding gas in the source leads to the production of gamma rays through the decay process $\pi^0 \to \gamma\gamma$. The acceleration of protons can occur at the termination shock, at which the jets collide with the ISM, or along the jet itself, allowing them to be transported to the lobe region. An upper limit on the diameter of the two lobes in the two-source model, $l \approx 40$ pc, is used to calculate the escape time. If we account for particle escape, the energy budget channelled in the accelerated proton population depends on the ratio between the particle (pp) cooling time and the escape time from the two lobes, $t_{\mathrm{pp}}/t_{\mathrm{esc}}$. The pp cooling time is defined as $t_{\mathrm{pp}} = 1/(n\sigma_{\mathrm{pp}}c) \approx 1.6 \times 10^{15}(n/1\,\mathrm{cm}^{-3})^{-1}$ s, in which σ_{pp} is the cross-section for pp interactions[67]. The escape time, $t_{\mathrm{esc}} \approx l^2/(2D(E))$, in which l is the source size, depends on the transport regime, $D(E)$. If we assume the diffusion at 1 PeV proceeds as inferred at GeV energies from the galactic secondary ratio, with $D(1\,\mathrm{PeV}) = \eta D_0 \approx \eta\,(3 \times 10^{30})\ \mathrm{cm}^2\,\mathrm{s}^{-1}$, then the escape time may be described as $t_{\mathrm{esc}} \approx 3 \times 10^9/\eta/(D_0/(3 \times 10^{30})\ \mathrm{cm}^2\,\mathrm{s}^{-1})$ s. Under this scenario, the energy budget required in accelerated protons above 1 PeV (1-PeV protons produce roughly 100–200-TeV photons) would be around 100% of the Eddington luminosity,

$$\begin{aligned}\dot{W}_{\mathrm{p}}(E_{\mathrm{p}} > 1\,\mathrm{PeV}) &= L_\gamma \frac{t_{\mathrm{pp}}}{t_{\mathrm{esc}}} \\ &\simeq 10^{39}\eta\left(\frac{L_\gamma}{10^{34}\ \mathrm{erg\ s^{-1}}}\right)\left(\frac{D_0}{3 \times 10^{30}\ \mathrm{cm^2\ s^{-1}}}\right)\left(\frac{n}{1\ \mathrm{cm^{-3}}}\right)^{-1}\ \mathrm{erg\ s^{-1}},\end{aligned} \tag{2}$$

in which n is the ambient gas density and $L_\gamma = 9.13\text{–}9.50 \times 10^{33}$ erg s^{-1} for the north and south lobes, respectively. Transport could proceed in a slower ($\eta < 1$) or faster ($\eta > 1$) way with respect to the galactic diffusion, D_0, derived from the cosmic-ray secondary ratio at GeV energies. Cosmic-ray transport in acceleration sites might also proceed much more slowly—in the extreme Bohm diffusion regime, $t_{\mathrm{esc}} \simeq 4 \times 10^3(E/1\,\mathrm{PeV})^{-1}$ years, in which the energy needed to be channelled into protons would be a small fraction of the Eddington luminosity.

VHE emission owing to leptonic interactions

In the leptonic scenario, when assuming that the continuously accelerated electrons follow a differential-power-law spectrum extending up to at least 200 TeV, the northern and southern gamma-ray sources may be produced by electrons with an energy budget of 7×10^{46} erg above 20 TeV in total. The fraction of the energy of electrons released in inverse Compton scattering and not lost to synchrotron cooling is determined by the ratio of the energy density of the magnetic field (proportional to B^2) to the energy density of target photons, such that the expected luminosity in hard X-rays from the HAWC lobes should be $L_X(>\text{few keV}) \approx L_{\mathrm{TeV}}(>1\,\mathrm{TeV})\left(\frac{B}{3\,\mu G}\right)^2 \approx (3-4) \times 10^{34}\left(\frac{B}{3\,\mu G}\right)^2$ erg s^{-1}. We note that this estimation assumes that the energy density of target photons is dominated by the cosmic microwave background, although the assumption may not be true in a small region close to the binary. Also, electron cooling may affect the electron spectrum and hence the expected X-ray luminosity.

Data availability

The datasets analysed during this study are available at a public repository maintained by the HAWC Collaboration (https://data.hawc-observatory.org).

Code availability

The study was carried out using the Multi-Mission Maximum Likelihood (3ML) HAWC Accelerated Likelihood (HAL) framework developed by the HAWC Collaboration. The software is open source and publicly available on Github at https://github.com/threeML/hawc_hal. The code distribution includes instructions on installation and use.

31. Albert, A. et al. Performance of the HAWC Observatory and TeV gamma-ray measurements of the Crab Nebula with improved extensive air shower reconstruction algorithms. *Astrophys. J.* **972**, 144 (2024).
32. Abeysekara, A. et al. Measurement of the Crab Nebula spectrum past 100 TeV with HAWC. *Astrophys. J.* **881**, 134 (2019).
33. Vianello, G. et al. The Multi-Mission Maximum Likelihood framework (3ML). Preprint at https://arxiv.org/abs/1507.08343 (2015).
34. Younk, P. W. et al. A high-level analysis framework for HAWC. In *Proc. 34th International Cosmic Ray Conference (ICRC2015)* 948 (2015).
35. Abeysekara, A. U. et al. Characterizing gamma-ray sources with HAL (HAWC accelerated likelihood) and 3ML. In *Proc. 37th International Cosmic Ray Conference (ICRC2021)* 828 (2022).
36. Atkins, R. et al. Observation of TeV gamma rays from the Crab Nebula with Milagro using a new background rejection technique. *Astrophys. J.* **595**, 803–811 (2003).
37. Abeysekara, A. et al. Observation of the Crab Nebula with the HAWC gamma-ray observatory. *Astrophys. J.* **843**, 39 (2017).
38. Ackermann, M. et al. Search for extended sources in the galactic plane using six years of Fermi-Large Area Telescope pass 8 data above 10 GeV. *Astrophys. J.* **843**, 139 (2017).
39. Kass, R. E. & Raftery, A. E. Bayes factors. *J. Am. Stat. Assoc.* **90**, 773–795 (1995).
40. Liddle, A. R. Information criteria for astrophysical model selection. *Mon. Not. R. Astron. Soc. Lett.* **377**, L74–L78 (2007).
41. Bozdogan, H. Model selection and Akaike's information criterion (AIC): the general theory and its analytical extensions. *Psychometrika* **52**, 345–370 (1987).
42. Abeysekara, A. et al. Extended gamma-ray sources around pulsars constrain the origin of the positron flux at Earth. *Science* **358**, 911–914 (2017).
43. Abeysekara, A. et al. HAWC observations of the acceleration of very-high-energy cosmic rays in the Cygnus Cocoon. *Nat. Astron.* **5**, 465–471 (2021).
44. Albert, A. et al. 3HWC: the third HAWC catalog of very-high-energy gamma-ray sources. *Astrophys. J.* **905**, 76 (2020).
45. Abdalla, H. et al. The H.E.S.S. Galactic plane survey. *Astron. Astrophys.* **612**, A1 (2018).
46. Abdollahi, S. et al. Incremental Fermi Large Area Telescope fourth source catalog. *Astrophys. J. Suppl. Ser.* **260**, 53 (2022).
47. Liu, Q. Z., van Paradijs, J. & van den Heuvel, E. P. J. Catalogue of high-mass X-ray binaries in the Galaxy. *Astron. Astrophys.* **455**, 1165–1168 (2006).
48. Liu, Q. Z., van Paradijs, J. & van den Heuvel, E. P. J. A catalogue of low-mass X-ray binaries in the Galaxy, LMC, and SMC (Fourth edition). *Astron. Astrophys.* **469**, 807–810 (2007).
49. Ritter, H. & Kolb, U. Catalogue of cataclysmic binaries, low-mass X-ray binaries and related objects (Seventh edition). *Astron. Astrophys.* **404**, 301–303 (2003).
50. Tanaka, Y. & Lewin, W. H. G. in *X-ray Binaries* (eds Lewin, W. H. G., van Paradijs, J. & van den Heuvel, E. P. J.) 126 (Cambridge Univ. Press, 1995).
51. Krivonos, R. et al. INTEGRAL/IBIS nine-year Galactic hard X-ray survey. *Astron. Astrophys.* **545**, A27 (2012).
52. Bird, A. et al. The IBIS soft gamma-ray sky after 1000 INTEGRAL orbits. *Astrophys. J. Suppl. Ser.* **223**, 15 (2016).
53. Oh, K. et al. The 105-month Swift-BAT all-sky hard X-ray survey. *Astrophys. J. Suppl. Ser.* **235**, 4 (2018).
54. Matsuoka, M. et al. The MAXI mission on the ISS: science and instruments for monitoring all-sky X-ray images. *Publ. Astron. Soc. Jpn.* **61**, 999–1010 (2009).
55. Shaw, A. et al. High resolution X-ray spectroscopy of V4641 Sgr during its 2020 outburst. *Mon. Not. R. Astron. Soc.* **516**, 124–137 (2022).
56. Revnivtsev, M., Gilfanov, M., Churazov, E. & Sunyaev, R. Super-Eddington outburst of V4641 Sgr. *Astron. Astrophys.* **391**, 1013–1022 (2002).
57. Koljonen, K. I. I. & Tomsick, J. A. The obscured X-ray binaries V404 Cyg, Cyg X-3, V4641 Sgr, and GRS 1915+105. *Astron. Astrophys.* **639**, A13 (2020).
58. Hjellming, R. et al. Light curves and radio structure of the 1999 September transient event in V4641 Sagittarii (=XTE J1819–254=SAX J1819.3–2525). *Astrophys. J.* **544**, 977 (2000).

59. Orosz, J. A. et al. A black hole in the superluminal source SAX J1819.3–2525 (V4641 Sgr). *Astrophys. J.* **555**, 489 (2001).
60. Chaty, S. et al. Optical and near-infrared observations of the microquasar V4641 Sgr during the 1999 September outburst. *Mon. Not. R. Astron. Soc.* **343**, 169–174 (2003).
61. Dame, T. M., Hartmann, D. & Thaddeus, P. The Milky Way in molecular clouds: a new complete CO survey. *Astrophys. J.* **547**, 792–813 (2001).
62. Dame, T. M. & Thaddeus, P. A CO survey of the entire northern sky. *Astrophys. J. Suppl. Ser.* **262**, 5 (2022).
63. Kalberla, P. M. et al. The Leiden/Argentine/Bonn (LAB) survey of galactic HI-final data release of the combined LDS and IAR surveys with improved stray-radiation corrections. *Astron. Astrophys.* **440**, 775–782 (2005).
64. Maitra, D. & Bailyn, C. D. X-ray observations of V4641 SGR (SAX J1819.3–2525) during the brief and violent outburst of 2003. *Astrophys. J.* **637**, 992 (2006).
65. Pahari, M., Misra, R., Dewangan, G. C. & Pawar, P. Constraining distance and inclination angle of V4641 Sgr using SWIFT and NuSTAR observations during low soft spectral state. *Astrophys. J.* **814**, 158 (2015).
66. Clemens, D. P. Massachusetts–Stony Brook galactic plane CO survey: the Galactic disk rotation curve. *Astrophys. J.* **295**, 422–428 (1985).
67. Gabici, S., Aharonian, F. A. & Casanova, S. Broad-band non-thermal emission from molecular clouds illuminated by cosmic rays from nearby supernova remnants. *Mon. Not. R. Astron. Soc.* **396**, 1629–1639 (2009).

Acknowledgements We acknowledge the support from: the US National Science Foundation (NSF); the US Department of Energy, Office of High Energy Physics; the Laboratory Directed Research and Development (LDRD) programme of Los Alamos National Laboratory; Consejo Nacional de Ciencia y Tecnología (CONACyT), México, grants 271051, 232656, 260378, 179588, 254964, 258865, 243290, 132197, A1-S-46288, A1-S-22784, CF-2023-I-645, cátedras 873, 1563, 341, 323, Red HAWC, México; DGAPA-UNAM grants IG101323, IN111716-3, IN111419, IA102019, IN106521, IN110621, IN110521, IN102223; VIEP-BUAP; PIFI 2012, 2013, PROFOCIE 2014, 2015; the University of Wisconsin Alumni Research Foundation; the Institute of Geophysics, Planetary Physics, and Signatures at Los Alamos National Laboratory; Polish Science Centre grant DEC-2017/27/B/ST9/02272; Coordinación de la Investigación Científica de la Universidad Michoacana; Royal Society – Newton Advanced Fellowship 180385; Generalitat Valenciana grant CIDEGENT/2018/034; the Program Management Unit for Human Resources & Institutional Development, Research and Innovation, NXPO (grant number B16F630069); Coordinación General Académica e Innovación (CGAI-UdeG), PRODEP-SEP UDG-CA-499; Institute of Cosmic Ray Research (ICRR), University of Tokyo; National Research Foundation of Korea (RS-2023-00280210). We also acknowledge the substantial contributions over many years of S. Westerhoff, G. Yodh and A. Z. Dominguez, all deceased members of the HAWC Collaboration. Thanks go to S. Delay, L. Díaz and E. Murrieta for technical support.

Author contributions X.W. and D.H. analysed the data and performed the maximum likelihood analysis. K.F. and S.C. carried out the physics modelling and interpretation. P.H., J.A.G. and B.L.D. helped to improve the manuscript. The full HAWC Collaboration has contributed to the construction, calibration and operation of the detector, the development and maintenance of reconstruction and analysis software, and the vetting of the analysis presented in this manuscript. All authors have reviewed, discussed and commented on the results and the manuscript.

Competing interests The authors declare no competing interests.

Additional information

Correspondence and requests for materials should be addressed to S. Casanova, K. Fang, D. Huang or X. Wang.

Peer review information *Nature* thanks the anonymous reviewers for their contribution to the peer review of this work.

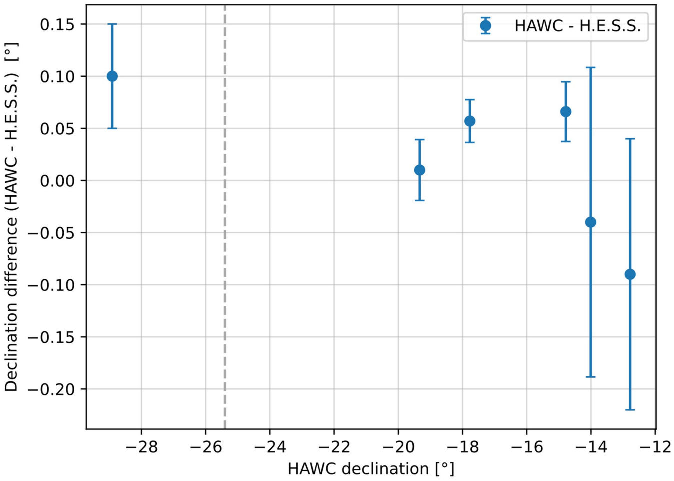

Extended Data Fig. 1 | The measured declination of HAWC sources. They are compared with the TeV counterpart measurements from the imaging atmospheric Cherenkov telescope experiment H.E.S.S. The vertical dashed line represents the declination of V4641 Sgr. The HAWC measurements generally agree with the source locations measured by H.E.S.S. within the provided uncertainties, covering a wide range of declinations, including extreme values. The error bars in the plot represent the uncertainties derived from the HAWC and H.E.S.S. errors added in quadrature, with the H.E.S.S. results taken from the HGPS paper[45].

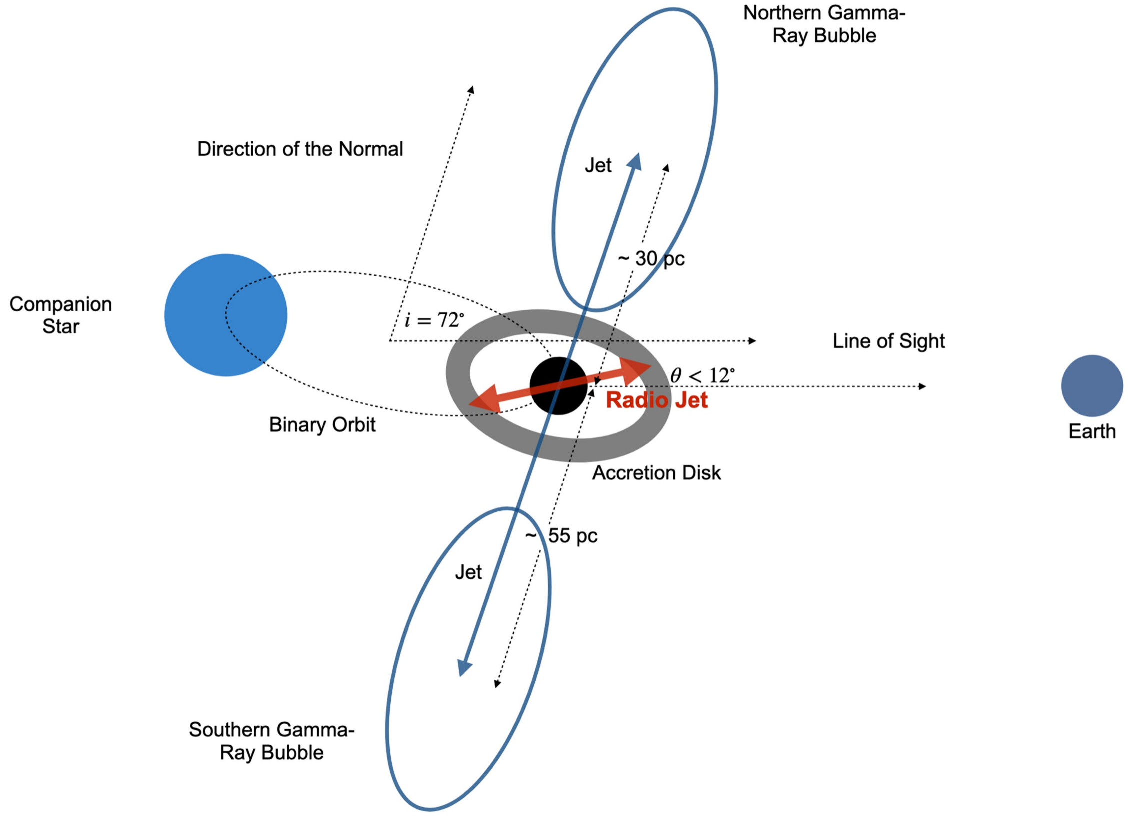

Extended Data Fig. 2 | Schematic illustration of V4641 Sgr. Red arrows indicate the radio-emitting and X-ray-emitting jets with sizes comparable with the scale of the binary system. They were detected during previous outbursts of this source with a jet inclination angle $\theta \lesssim 12°$ (ref. 59). Blue arrows indicate a set of gamma-ray-emitting jets suggested by this work, extending approximately 100 pc and oriented perpendicular to the accretion disk.

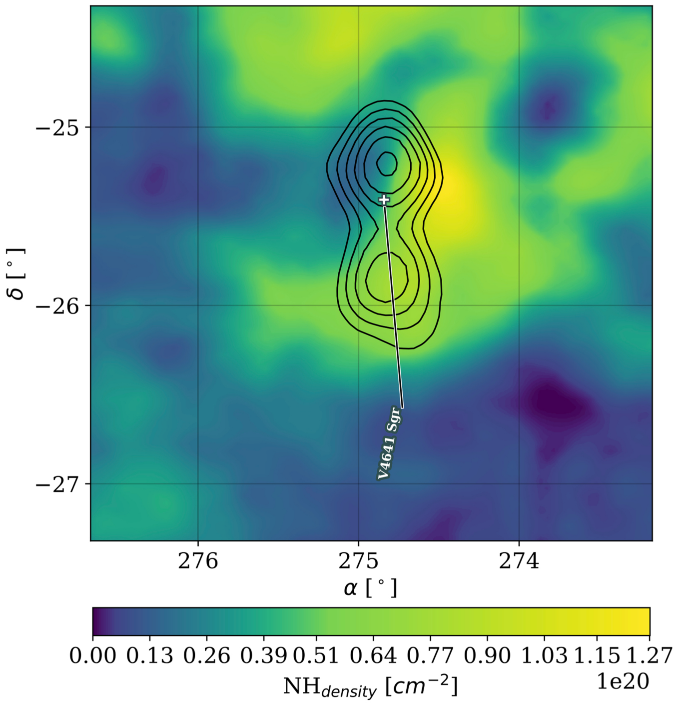

Extended Data Fig. 3 | Gas distribution at the location of V4641 Sgr. The black contours represent the VHE gamma-ray excess obtained by HAWC. The column density of atomic hydrogen, N_{H}, at the V4641 Sgr location is obtained by integrating the gas survey cubes over the range 70–120 km s^{-1} and then dividing by the velocity interval. The level of noise in the molecular hydrogen map is too high to confirm or rule out the presence of the target material in molecular form.

Extended Data Table 1 | Comparison of the performance of different models

Model	−logLikelihood	BIC	AIC
One Point Source	60733	121520	121473
One Asymmetric Extended Source	60694	121485	121403
Two Point Sources	60694	121498	121404

Three models are evaluated using three criteria: negative log-likelihood, BIC and AIC.

Extended Data Table 2 | Best-fit parameters for the asymmetric extended-source model

R.A. [°]	Dec. [°]	Gaussian Width of Major Axis [°]	ϕ_0 [$\times 10^{-16}\mathrm{cm}^{-2}\mathrm{TeV}^{-1}\mathrm{s}^{-1}$]	Index	Pivot Energy [TeV]
274.81 ± 0.03	-25.56 ± 0.09	0.54 ± 0.08	$4.5^{+0.7}_{-0.6}$	-2.1 ± 0.1	57

This table presents the key parameters of the asymmetric extended-source model, detailing its spatial and spectral characteristics. These include its location in right ascension (RA) and declination (Dec), the flux normalization and spectral index, as well as its pivot energy.

Extended Data Table 3 | Data selected for the X-ray outbursts according to the Bayesian analysis of the daily light curves from the MAXI public data

Data selected according to MAXI	Number of Days
Oct 4–Nov 7, 2021 (MJD 59491–59525)	35
Jan 12–Apr 1, 2020 (MJD 58860–58940)	80
Aug 30–Oct 9, 2018 (MJD 58360–58400)	40
Jul 22–Aug 16, 2015 (MJD 57225–57250)	25
Total days	180

Table showing specific observation periods and the corresponding number of days for each. The data span a total of 180 days, with each date range listed alongside the modified Julian date (MJD) for reference.